



A Micromolding Method for Transparent and Flexible Thin-Film Supercapacitors and Hybrid Supercapacitors

Tian Liu, Runyu Yan, Haijian Huang, Long Pan, Xiaobao Cao, Andrew deMello, and Markus Niederberger*

Thin-film supercapacitors are promising candidates for energy storage in wearable electronics due to their mechanical flexibility, high power density, long cycling life, and fast-charging capability. In addition to all of these features, device transparency would open up completely new opportunities in wearable devices, virtual reality or in heads-up displays for vehicle navigation. Here a method is introduced for micromolding Ag/porous carbon and Ag/Ni_xFe_yO_z@reduced graphene oxide (rGO) into grid-like patterns on polyethylene terephthalate foils to produce transparent thin-film supercapacitors and hybrid supercapacitors. The supercapacitor delivers a high areal capacitance of 226.8 μF cm⁻² at a current density of 3 μA cm⁻² and with a transparency of 70.6%. The cycling stability is preserved even after 1000 cycles under intense bending. A hybrid supercapacitor is additionally fabricated by integrating two electrodes of Ag/porous carbon and Ag/Ni_xFe_yO_z@rGO. It offers an areal capacitance of 282.1 μF cm⁻² at a current density of 3 μA cm⁻², a transparency of 73.3% and the areal capacitance only decreases slightly under bending. This work indicates that micromolding of nano- and micro-sized powders represents a powerful method for preparing regular electrode patterns, which are fundamental for the development of transparent energy storage devices.

1. Introduction

Transparent electronics has been in the focus of intensive worldwide research activities in industry as well as in academia. A fascinating property of transparent electronic devices is that they provide virtual images overlaid on a real-world scene. This unique feature opens up entirely new applications in consumer electronics, most notably displays, but also

in virtual/augmented reality, wearable devices and vehicle navigation information. Independent of the precise application, transparent electronic devices must be powered by an energy source. In the ideal case, the energy storage device is fully integrated in the electronic device, and thus must also be transparent. A promising class of energy storage devices for such next-generation electronics is the supercapacitor. In addition to high-power densities, long cycling life, and rapid charge-discharge rates,^[1] thin-film supercapacitors offer unique physical properties, such as mechanical flexibility and/or optical transparency, which greatly expand their application potential.^[1a,2] The primary challenges when fabricating transparent thin-film supercapacitors relate to the electrode materials (for both the active material and current collector), with their smallest structural dimension needing to be below the optical absorption thickness of the material. Accord-

ingly, a popular strategy for making transparent devices is to ensure that the thickness of the active material(s) is less than their optical absorption length.^[3] For example, thin layers of conductive graphene,^[4] poly(3,4-ethylenedioxythiophene)-poly(styrenesulfonate) (PEDOT:PSS)^[5] and pseudocapacitor nanoparticles such as Co₃O₄,^[6] or MnO₂^[7] have been employed as transparent electrodes in supercapacitors. However, it is evident that in such an approach the mass loading of the current collector and active material must be low to keep the film thin and thus transparent, resulting in a highly limited areal capacitance. To tackle this problem, efforts are being made toward new designs that offer high transparency. One promising approach is to fabricate a micro-structured electrode composed of patterned active materials and current collectors. A patterned electrode grid that covers only a small fraction of the whole surface area significantly increases the transparency of the electrode. Different approaches have been reported for producing high capacitance materials for transparent electrodes, whilst maintaining high areal capacitance and reasonable energy density. Examples include random networks of metal nanowires^[8] or self-assembled gold nanorime mesh conductors (with 66.7% transmittance for the single electrode) that yield skin-thin, transparent and stretchable supercapacitors. Indeed, such supercapacitors exhibit 55% transmittance at 550 nm and a maximum energy density of 3.8 mWh cm⁻³

T. Liu, Dr. H. Huang, Dr. L. Pan, Prof. M. Niederberger
Laboratory for Multifunctional Materials
Department of Materials
ETH Zürich
Vladimir-Prelog-Weg 5, Zürich 8093, Switzerland
E-mail: markus.niederberger@mat.ethz.ch

Dr. R. Yan
Department of Colloid Chemistry
Max Planck Institute of Colloids and Interfaces
Am Mühlenberg 1, Potsdam 14476, Germany

Dr. X. Cao, Prof. A. deMello
Institute for Chemical and Bioengineering
Department of Chemistry and Applied Biosciences
Vladimir-Prelog-Weg 1, Zürich 8093, Switzerland

The ORCID identification number(s) for the author(s) of this article can be found under <https://doi.org/10.1002/adfm.202004410>.

DOI: 10.1002/adfm.202004410

at a power density of 4043 mWh cm⁻³.^[9] Additionally, Huang et al. developed a transparent film composed of a Fe₂O₃ nanowire network wrapped in graphene shells for use as transparent electrodes. At 550 nm, the transmittance of a single electrode is ≈62.5%, which decreases to 42.9% for the corresponding assembled supercapacitor.^[10] These films have a power density of 191.3 W cm⁻³ and an energy density of 8 mWh cm⁻³, which is comparable to that of lithium-ion thin-film batteries. All the above examples, however, suffer from the problem that the transparency of the full cell decreases significantly upon stacking the two electrodes due to their random structure.^[3a] To maximize the transparency of a complete full cell, it is therefore essential to pattern the two electrodes into regular grids and perfectly align them during battery assembly. To ensure good electrochemical stability of the supercapacitor, a layer of highly conductive metal (e.g., Ag^[8d,11] or Au^[8b,12] as current collectors) must be integrated with the active materials, which makes the design of the electrode architecture significantly more challenging. To this end, Xu et al. reported a regular and transparent metallic mesh electrode decorated with active MnO₂ microstructures, which was produced by lithography and electrodeposition methods and served as a transparent and foldable supercapacitor electrode.^[13] Unfortunately, the fraction of the occupied electrode area increased upon addition of the active material, since MnO₂ could only be electrodeposited around the Au pattern, lowering the transparency of the metal mesh. Additionally, electrodeposition significantly limits the range of accessible active materials. Accordingly, an ideal method should be able to micropattern a broad range of materials into regular grids, integrating both the current collector and active material for optimized transparency.

In this work we present a micromolding method, which can be applied to different materials, and makes it possible to fabricate two types of transparent energy storage devices, namely thin-film supercapacitors and hybrid supercapacitors. As electrode materials, we use ordered mesoporous carbon, which we recently introduced as symmetric electrodes for supercapacitors.^[14] Mesoporous carbon is a highly attractive candidate for electric double-layer capacitors (EDLC), delivering high gravimetric capacitance (133 F g⁻¹ at 0.1 A g⁻¹) and good capacitance retention under high-power conditions (126 F g⁻¹ at 40 A g⁻¹). Although supercapacitors exhibit rapid power delivery via fast non-Faradaic surface ion adsorption/desorption, they still suffer from low energy density, because charges are only stored physically on the surface.^[15,16] One way to solve this problem is to design hybrid energy-storage devices that possess both high energy and power density. Therefore, we recently investigated a Ni_xFe_yO_z@reduced graphene oxide (rGO) composite as a high-power anode for lithium-ion hybrid supercapacitors.^[15] The transparent and flexible Ag/porous carbon electrodes featuring a hexagonal grid structure were fabricated via direct micromolding of porous carbon on top of a regular Ag pattern. The grid shape strongly influences the transparency. Theoretical studies of triangular, square and hexagonal patterns showed that the hexagonal grid unit offered the highest light transmission limit. In addition, it was the one least affected by an increase in line width.^[17] Our approach provides good contact between the current collector and the active materials, with the fraction of the occupied electrode area remaining

unchanged due to the compact two-layer architecture. The thin-film supercapacitors are assembled by sandwiching a gel-electrolyte between two transparent Ag/porous carbon electrodes. For the lithium-ion hybrid supercapacitor, the Ni_xFe_yO_z@rGO composite was patterned on the hexagonal Ag grid. The hybrid supercapacitor, integrating two transparent electrodes of Ag/porous carbon and Ag/Ni_xFe_yO_z@rGO, offered high transparency, long cycle life and higher energy density and power density than the thin-film supercapacitor.

2. Results and Discussion

Figure 1a summarizes the different steps for patterning transparent electrodes over a large area of 3 × 3 cm² by the micromolding method. First, a polydimethylsiloxane (PDMS) stamp with a hexagonal pattern (side length $a = 200 \mu\text{m}$, width $w = 20 \mu\text{m}$ and height $h = 50 \mu\text{m}$) and with the appropriate flexibility and hardness was produced photolithographically (Figure S1, Supporting Information). The PDMS stamp and the polyethylene terephthalate (PET) substrate were cleaned by O₂ plasma to enhance surface hydrophilicity. The two layers were then attached firmly to each other by applying pressure onto the PDMS stamp (Figure 1b and Figure S2, Supporting Information), which is maintained during patterning. In the next step, Ag ink was deposited around the edges of the PDMS stamp and by capillary force drawn into the channels. In this regard, it is important that the channels are open at the substrate edge and accessible to the ink. Without removing the stamp, the Ag ink was dried at 130 °C to ensure high conductivity (Figure 1c). At this stage of the process, the channels are not completely filled and still have some space for the active material. The aqueous electrode ink is also hydrophilic, and therefore flows easily into the O₂ plasma-treated PDMS channels, resulting in a second layer on top of the dried Ag nanoparticles (Figure 1d). Finally, the stamp was carefully removed, with the bilayer of Ag current collector and electrode material remaining on the PET substrate, forming a transparent and flexible electrode.

Scanning electron microscopy (SEM) images of the microstructured Ag are presented in Figure 2a. The Ag pattern is distributed uniformly over a large area of the PET substrate, with the feature sizes matching those of the PDMS stamp. Theoretical transmission is calculated as the ratio of the uncovered area to the total area, which can be expressed^[18] as $T = \left[\frac{b-w}{b} \right]^2 = 89.4\%$ (spacing distance $b = 366 \mu\text{m}$, width $w = 20 \mu\text{m}$) (Figure 2a). The SEM images in Figure 2d and Figure S4a (Supporting Information) reveal the magnified sides of the hexagons and the spherical morphology of the Ag nanoparticles with particle diameters ranging from 50–100 nm. The X-ray powder diffraction (XRD) pattern (Figure S3a, Supporting Information) shows that the diffraction peaks match well with the cubic phase of Ag (JCPDS card No. 04-0783).^[19]

The sheet resistance of the patterned Ag film (2 × 2 cm²) was measured as a function of the annealing temperature (Figure S3b, Supporting Information), indicating that the Ag film achieves 76 Ω sq⁻¹ after sintering for 1 h at 130 °C, which is ideal for a current collector in a supercapacitor. According to the SEM analysis, the Ag nanoparticles form a relatively loosely

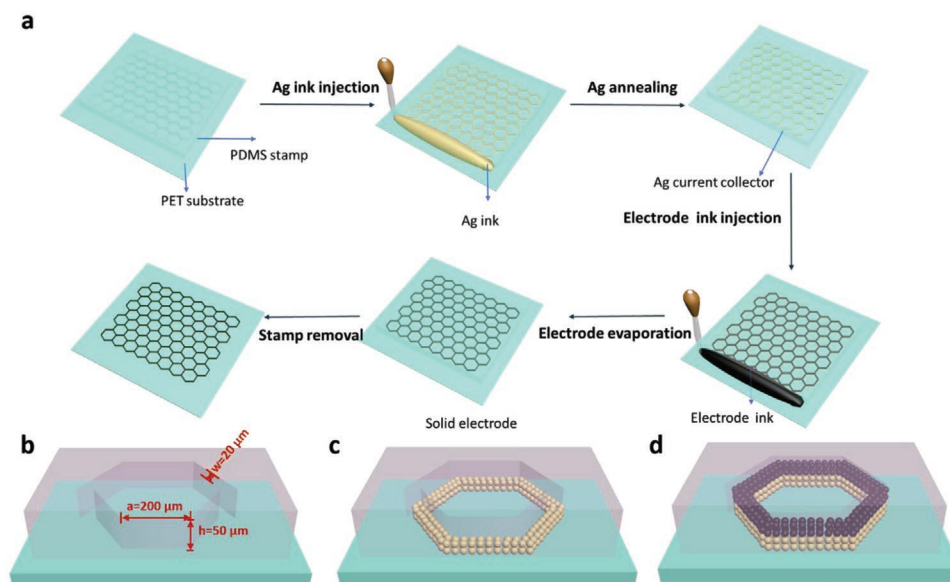


Figure 1. Schematic illustration of the different steps used to prepare transparent and flexible current collector-active material bilayer electrodes.

connected layer prior to sintering (Figure S4a, Supporting Information). After heat treatment, the Ag nanoparticles are sintered to form a continuous network of larger particles, which is essential to ensure low sheet resistance (Figure S4b, Supporting Information). A 3D topography image measured using an optical profilometer (Figure S5a, Supporting Information) confirms the high definition and homogeneity of the hexagonal Ag grid. The evaporation-induced deposition of porous carbon or $\text{Ni}_x\text{Fe}_y\text{O}_z@\text{rGO}$ on top of the Ag pattern has no influence on the quality of the grids, which clearly maintain their original shape as evidenced by SEM images in Figure 2b,e,c,f, respectively. Magnified SEM images reveal the morphology of the micro-sized porous carbon and the wrinkled $\text{Ni}_x\text{Fe}_y\text{O}_z@\text{rGO}$ composite layer on top of the Ag grids (Figure S6a,b, Supporting Information). The optical transmittance of the PET substrate at the wavelength of 550 nm is 91.6% (Figure S7a, Supporting Information), while for Ag, Ag/porous carbon and Ag/ $\text{Ni}_x\text{Fe}_y\text{O}_z@\text{rGO}$ it is 87.9%, 84.2%, and 86.3%, respectively (Figure 2g). By introducing the active material as the second layer (on top of the Ag film) the transmittances of Ag/porous carbon and Ag/ $\text{Ni}_x\text{Fe}_y\text{O}_z@\text{rGO}$ films drop slightly due to the increased thickness. Additionally, the bilayer films appear slightly darker than the Ag film, as shown in the digital images (inset, Figure 2g). The thicknesses of 3, 4, and 5 μm for the Ag, Ag/ $\text{Ni}_x\text{Fe}_y\text{O}_z@\text{rGO}$ and Ag/porous carbon films, respectively, are visible in the surface profile in Figure S5b (Supporting Information).

In the last step of device fabrication, the two electrodes must be combined into the Ag/porous carbon||Ag/porous carbon supercapacitor by aligning both patterns with each other to achieve high transparency, as shown in Figure 2h. A photograph of the final transparent and flexible thin-film supercapacitor is shown in Figure 3a. The assembled full cell exhibits a transmittance of 70.6% at the wavelength of 550 nm at an angle of 90° between the direction of the light and the device. If the supercapacitor is tilted by 30° and 60° with respect to its

original position, its transmittance remains nearly the same with 70.7% and 70.0%, respectively (Figure S7b, Supporting Information). The slight changes might be due to minor shadowing and diffraction effects from the grid. Nevertheless, the transmittance remains almost unaffected by tilting of the device. If the position of the two electrodes is not well aligned during their combination, the transmittance is significantly reduced. Figure S8a (Supporting Information) shows the results for two supercapacitors with two different, but defined types of misalignments of the two electrodes (labeled as “Misaligned 1” and “Misaligned 2”), resulting in transmittance values of 62.5% and 46.8%, respectively. The optical microscopy images in Figure S8c,d (Supporting Information) display the corresponding misaligned arrangements. For comparison, Figure S8b (Supporting Information) shows the optical microscopy image of the aligned stack of electrodes with a transmittance of 70.6% (Figure 3b). As a third misaligned structure (labeled as “Misaligned 3”) we chose a completely random stack of electrodes (Figure S8e,f, Supporting Information). Such a non-specific misaligned arrangement typically exhibits a transmittance of about 35% (Figure 3b). Despite the careful alignment of the two electrodes in the full cell device, it offers a lower transmittance compared to the single electrodes due to unavoidable small mismatches between the two stacked electrodes.

Figure S9 (Supporting Information) shows a schematic illustration of the full cell with a poly(vinylidene fluoride-co-hexafluoropropylene) (PVDF-HFP)/tetraethylammonium tetrafluoroborate (Et_4NBF_4) gel electrolyte sandwiched in between Ag/porous carbon||Ag/porous carbon electrodes. The electrochemical conductivity of the gel electrolyte was tested using electrochemical impedance spectroscopy (EIS) at open circuit potential and frequencies between 10 mHz to 100 kHz (Figure S10a, Supporting Information). The equivalent electrical circuit used for fitting the EIS measurements are shown in Figure S10c (Supporting Information). The bulk resistance (R_b) and the charge transfer resistance (R_{ct}) of the electrolyte

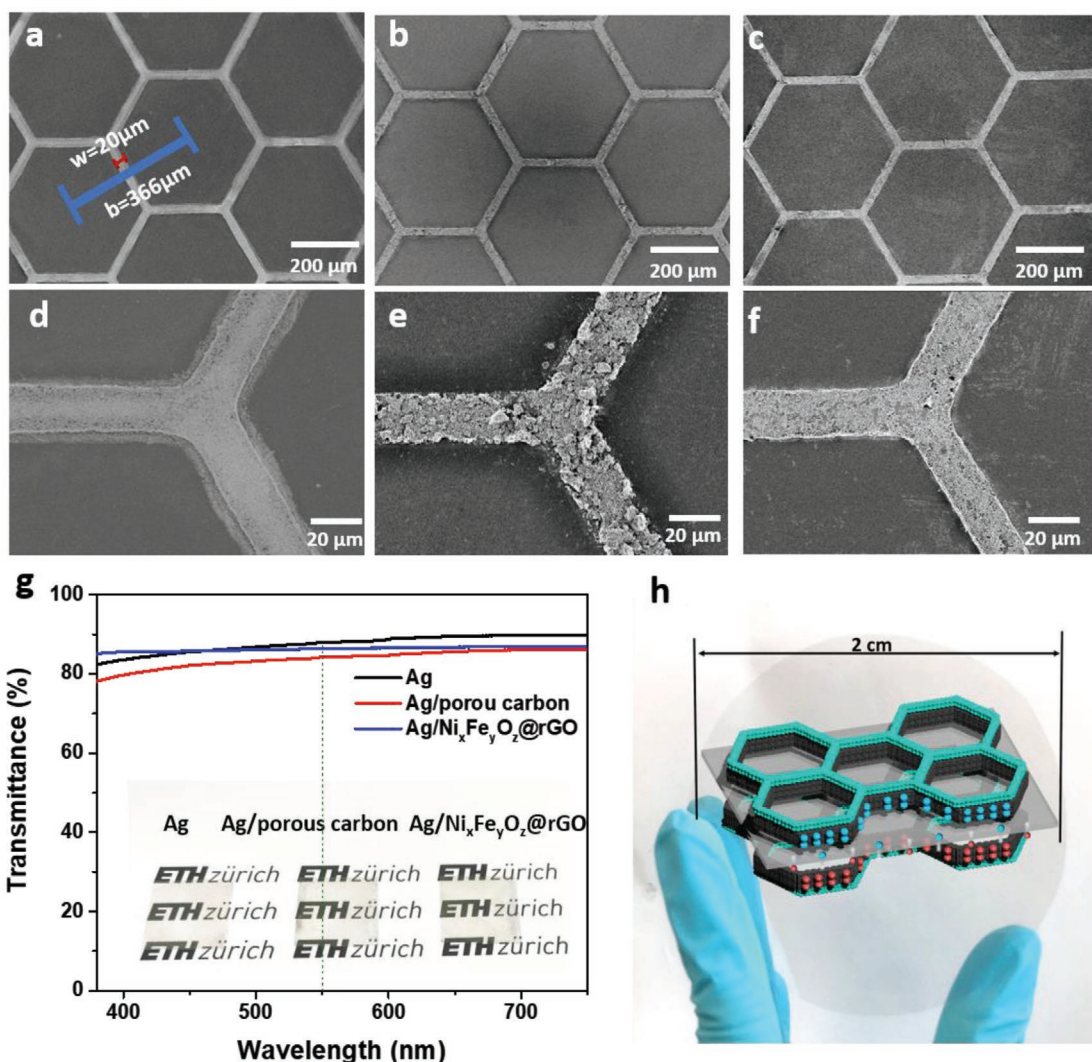


Figure 2. SEM images of the microstructured a) Ag, b) Ag/porous carbon and c) Ag/Ni_xFe_yO_z@rGO patterns; SEM images at higher magnification of d) Ag, e) Ag/porous carbon and f) Ag/Ni_xFe_yO_z@rGO patterns; g) Optical transmittance of Ag, Ag/porous carbon and Ag/Ni_xFe_yO_z@rGO films and the corresponding digital photographs (inset); h) Schematic illustration of the sandwich structure of the transparent and flexible supercapacitor/hybrid supercapacitor.

are estimated to be 1.12 and 15.88 Ω, respectively. The ionic conductivity (σ) of the gel electrolyte is calculated to be 5.9 mS cm⁻¹ from the bulk resistance according to Equation (1) (Experimental Section).

The galvanostatic charge-discharge (GCD) plots of the transparent supercapacitor exhibit high symmetry and linear slopes at areal current densities of 3, 60, and 120 μA cm⁻² (Figure 3c). The voltage drops at a current density of 60 (0.21 V) and 120 μA cm⁻² (0.34 V) are higher than those at 3 μA cm⁻² (nearly 0 V), indicating surface polarization and contact resistance effects. The corresponding areal capacitances, energy densities and power densities are summarized in Figure 3f. Cyclic voltammetry (CV) was used to determine the capacitive performance of the supercapacitor under a variety of scan rates (10–100 mV s⁻¹), with a potential window ranging from 0 to 2.5 V (Figure 3d). The rectangular and symmetric nature of the CV curves indicate that the porous carbon-based supercapacitor

has excellent EDLC behavior with an extremely rapid current response on voltage reversal, as previously reported.^[14,20] The drop in areal capacitance was only 13.3% after testing over 1000 cycles at a current density of 60 μA cm⁻², with a Coulombic efficiency of 99.9% (Figure 3e). Moreover, the transmittance is hardly affected by the electrochemical reactions. According to Figure S7c (Supporting Information), the transmittance of the supercapacitor is 69.9% after 1000 cycles at the current density of 60 μA cm⁻² compared to 70.6% before cycling.

In addition to a transparent supercapacitor, we also fabricated and tested a lithium-ion hybrid supercapacitor. In comparison to supercapacitors, hybrid supercapacitors are more complex in design, since two electrodes composed of different materials must be combined. A Ni_xFe_yO_z@rGO composite was employed as the anode. The morphology of the composite Ni_xFe_yO_z@rGO in Figure 4a shows a structure similar to a wrinkled sheet of paper with the Ni_xFe_yO_z nanoparticles

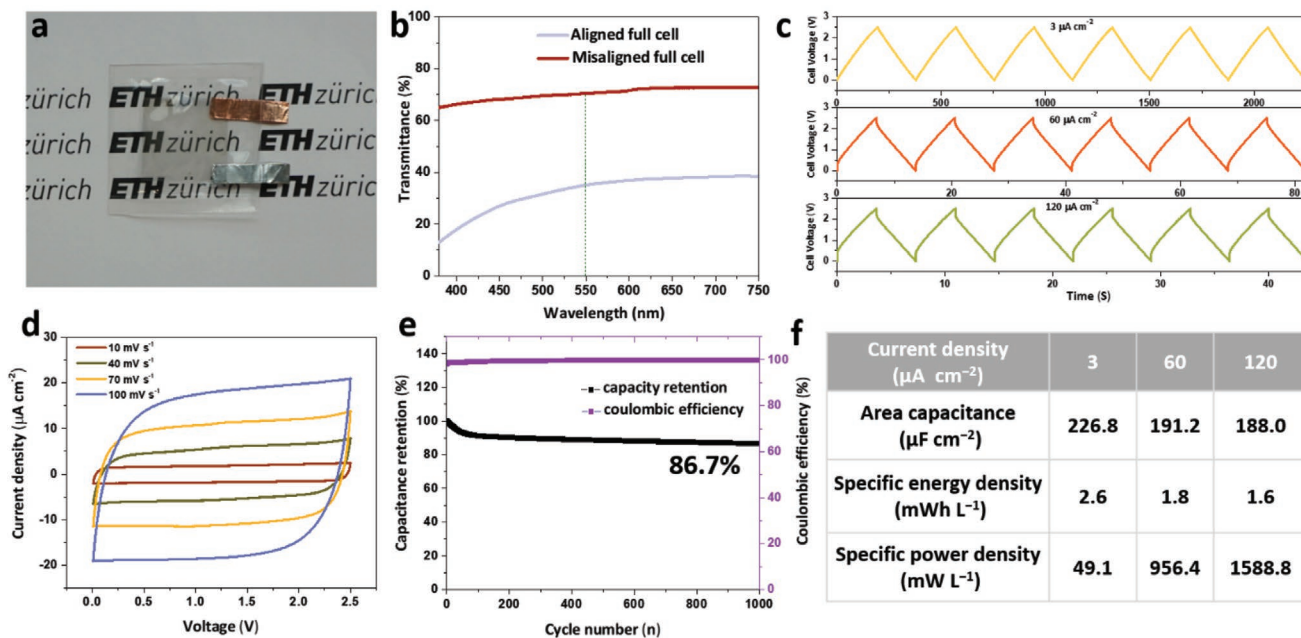


Figure 3. a) Photograph of the fully assembled transparent and flexible thin-film supercapacitor; b) Optical transmittance of the supercapacitor composed of aligned and randomly misaligned electrodes; c) GCD plots of the supercapacitor at current densities of 3, 60, and $120 \mu\text{A cm}^{-2}$; d) CV curves of the supercapacitor for scan rates of 10, 40, 70, and 100 mV s^{-1} ; e) Cycling performance of the supercapacitor at a cycling rate of $60 \mu\text{A cm}^{-2}$; f) Areal capacitances, energy densities and power densities of the supercapacitor at current densities of 3, 60, and $120 \mu\text{A cm}^{-2}$.

uniformly distributed on the surface of the rGO sheets. The element distribution map acquired by TEM and using a high-angle annular dark-field detector (HAADF) further confirms

that Ni and Fe are homogeneously distributed over the rGO sheets. The electrochemical performance was first studied in half-cells, fabricated by directly using the $\text{Ni}_x\text{Fe}_y\text{O}_z@\text{rGO}$

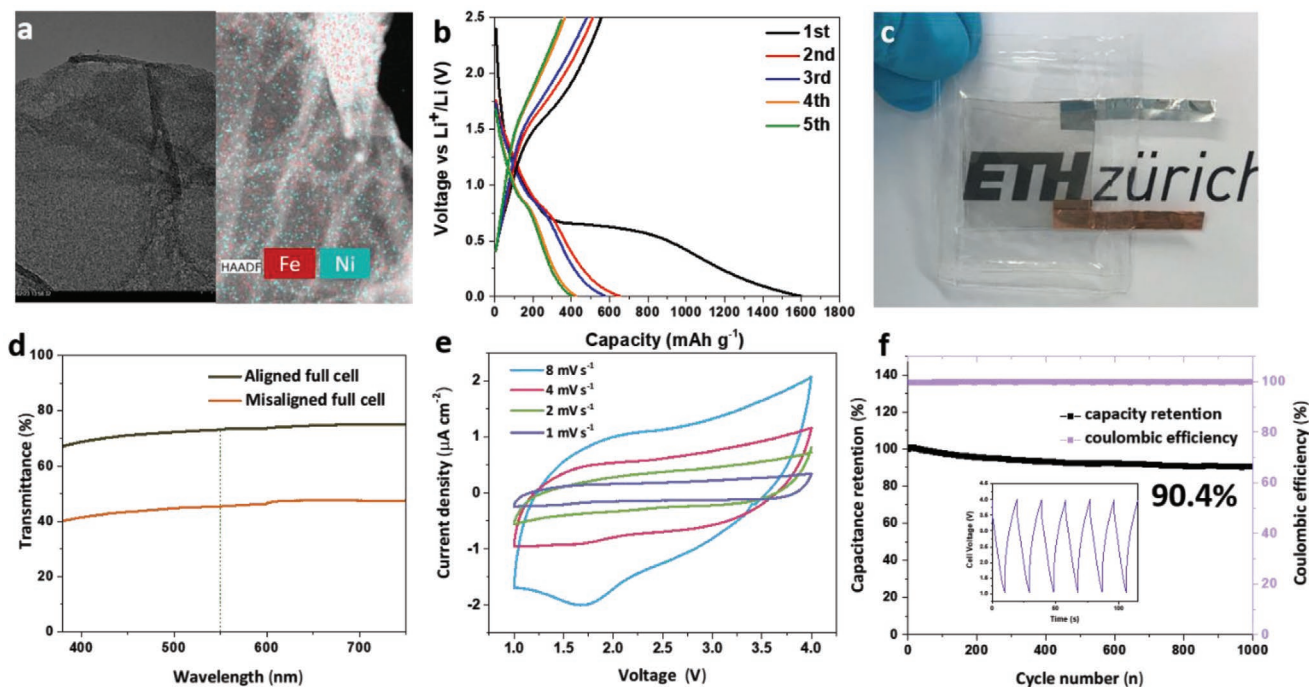


Figure 4. a) TEM and HAADF images with element distribution map of $\text{Ni}_x\text{Fe}_y\text{O}_z@\text{rGO}$ composite; b) GCD profiles at 0.1 A g^{-1} ; c) Photograph of the assembled transparent and flexible thin-film hybrid supercapacitor; d) Optical transmittance of hybrid supercapacitor with aligned and misaligned electrodes; e) CV curves of the hybrid supercapacitor for scan rates of 1, 2, 4, and 8 mV s^{-1} ; f) Cycling performance of the hybrid supercapacitor at a cycling rate of $60 \mu\text{A cm}^{-2}$ and GCD plot at current densities of $60 \mu\text{A cm}^{-2}$ (inset).

composite as one electrode and lithium foil as the counter and reference electrode. The disordered, nearly amorphous structure of $\text{Ni}_x\text{Fe}_y\text{O}_z@\text{rGO}$ was confirmed by powder X-ray diffraction measurements (Figure S11a, Supporting Information), in agreement with previous studies.^[15] Figure 4b shows the first five GCD profiles of the $\text{Ni}_x\text{Fe}_y\text{O}_z@\text{rGO}$ composite at a current density of 0.1 A g^{-1} . The initial capacity loss is presumably a result of the high surface area, which facilitates irreversible lithium loss due to the formation of a solid electrolyte interphase (SEI) layer and the decomposition of the electrolyte. The composite displays a potential plateau at around 0.8 V , corresponding to the reduction of Ni^{2+} to Ni^0 and Fe^{3+} to Fe^0 inside the Li_2O matrix.^[15] The CV curves of the composite at sweep rates ranging from 0.2 to 1 mV s^{-1} reveal the same reduction plateau (Figure S11b, Supporting Information). Figure S11c (Supporting Information) shows the rate performance of the composite at current densities ranging from 0.1 to 2 A g^{-1} . A high specific capacity of 800 mA h g^{-1} can be retained at 0.1 A g^{-1} . After 500 cycles at a current density of 2 A g^{-1} , the capacity is 448 mA h g^{-1} with a Coulombic efficiency of 99.1%, confirming that this composite is indeed promising as a high-performance anode for lithium-ion hybrid supercapacitors (Figure S11d, Supporting Information).

For the hybrid supercapacitor we used another electrolyte than for the supercapacitor. A transparent PVDF-HFP/lithium bis (trifluoromethanesulfonyl) imide (LiTFSI) gel electrolyte with an ionic conductivity of 5.75 mS cm^{-1} was prepared (Figure S10b, Supporting Information). For the hybrid supercapacitor, the PVDF-HFP/LiTFSI gel electrolyte was sandwiched between the $\text{Ag}/\text{Ni}_x\text{Fe}_y\text{O}_z@\text{rGO}||\text{Ag}/\text{porous carbon}$ electrodes (Figure 4c). The transmittance of the hybrid supercapacitor with well-aligned electrodes at 550 nm is up to 73.3%, while for randomly misaligned electrodes the value drops to 45.3% (Figure 4d). Tilting experiments analogous to those performed with the supercapacitor resulted in transmittances of 74.5% and 72.8% for angles of 30° and 60° (Figure S7b, Supporting Information), indicating that similar to the behavior of the supercapacitor also the transmittance of the hybrid device is nearly independent from the viewing angle. The CV curves in Figure 4e show typical quasi-rectangular shapes. Deviation from the ideal rectangular shape at all scan rates implies the coexistence of a conversion-type energy storage mechanism for the structurally disordered $\text{Ni}_x\text{Fe}_y\text{O}_z$ nanoparticles. According to Figure 4f, the areal capacitance of the hybrid supercapacitor is well maintained up to 1000 cycles, with a capacitance retention of 90.4% at a current rate of $60 \mu\text{A cm}^{-2}$ and Coulombic efficiency of 99.9%. From the inset image of the GCD profiles, the areal capacitance, energy density and power density at a current density of $60 \mu\text{A cm}^{-2}$ are calculated to be $226.4 \mu\text{F cm}^{-2}$, 2.7 mWh L^{-1} , and $1002.5 \text{ mWh L}^{-1}$, respectively. Table S1 (Supporting Information) shows that the hybrid supercapacitor delivers higher areal capacitances, energy densities and power densities compared to the supercapacitor at current densities of 3, 60, and $120 \mu\text{A cm}^{-2}$, respectively. Also for the hybrid supercapacitor, the transmittance hardly changes during cycling. It remains at 72.4% after 1000 cycles at the current density of $60 \mu\text{A cm}^{-2}$ (Figure S7c, Supporting Information).

To further explore the suitability of our devices in applications such as transparent flexible sensors, roll-up displays

or wearable electronics, bending properties were characterized by measuring the CV curves and cycling performance under different bending conditions. The mechanical flexibility of the transparent Ag current collector was first investigated by bending tests (Figure S12, Supporting Information). The change in resistance of the Ag film can be expressed as $(R - R_0)/R_0$, where R_0 is the initial resistance ($= 7.6 \Omega \text{ sq}^{-1}$), and R is the resistance obtained when the sample was bent to a radius of 6 mm. Due to the generation of cracks, the initial sheet resistance increased by 48% under tension bending condition ($11.2 \Omega \text{ sq}^{-1}$) and by 46% under compression bending condition ($11.0 \Omega \text{ sq}^{-1}$) after 500 cycles.^[21] Figure 5a shows the experimental set-up with the nonbent sample used as a reference. Bending tests for the supercapacitor and hybrid supercapacitor were performed under bending radii of $r_1 = 9 \text{ mm}$, $r_2 = 6 \text{ mm}$, and $r_3 = 3 \text{ mm}$, respectively (Figure 5b–d). The two opposite sides of the sample were fixed onto the plastic plate. The different bending radii were achieved by moving the bar on the right-hand side, followed by fixing it with a metallic screw. Independent of the bending radius, the supercapacitor retained rectangular-shaped CV curves, indicating stable capacitive behavior even under high mechanical stress (Figure 5e). Indeed, the performance of the supercapacitor was tested at a bending radius of 6 mm for 1000 cycles, with the capacitance remaining at 83.7% (Figure 5f). This value is close to that of the unbent device (86.7%), which means that the supercapacitor performs stably even under harsh mechanical conditions. The cycle stability may be ascribed to the good contact between the Ag current collector and porous carbon, with the soft gel electrolyte partially protecting the electrode patterns during bending.^[22] Similar bending tests were also performed on the transparent hybrid supercapacitor. The CV curves of the bent device show the same shape as the flat hybrid supercapacitor (Figure 5g). The electrochemical stability of the hybrid supercapacitor was tested under the bending radius of 6 mm, as shown in Figure 5h. The capacitance remained at 88.2% after 1000 cycles, indicating that the hybrid supercapacitor is flexible enough to operate in a bent state. When the bending conditions are further aggravated by reducing the radius to 3 mm, the supercapacitor and the hybrid supercapacitor delivered a capacitance of 81.4% and 93.1%, respectively, of the initial values after 1000 cycles (Figure S13, Supporting Information).

Summarizing these experiments, it can be concluded that the supercapacitor and hybrid supercapacitor prepared by the micromolding method exhibit excellent electrochemical performance and mechanical flexibility, which makes them in combination with the high optical transparency appealing for “see-through” or “invisible” electronic applications.

Figure 6 shows the volumetric Ragone plots of the supercapacitor and hybrid supercapacitor. The two devices were cycled at current densities of 3, 30, 60, 120, and $240 \mu\text{A cm}^{-2}$ to obtain the values for the energy and power densities. The supercapacitor provides the highest energy density of 2.6 mWh L^{-1} at a power density of 49.1 mW L^{-1} . Increasing the power density to 1588.8 mW L^{-1} still results in an energy density of 1.6 mWh L^{-1} . For the hybrid supercapacitor, the energy density reaches 3.9 mWh L^{-1} at a specific power of 54.2 mW L^{-1} , and maintaining 2.2 mWh L^{-1} when the specific power increases to 1975.9 W L^{-1} . There is a considerable amount of data available

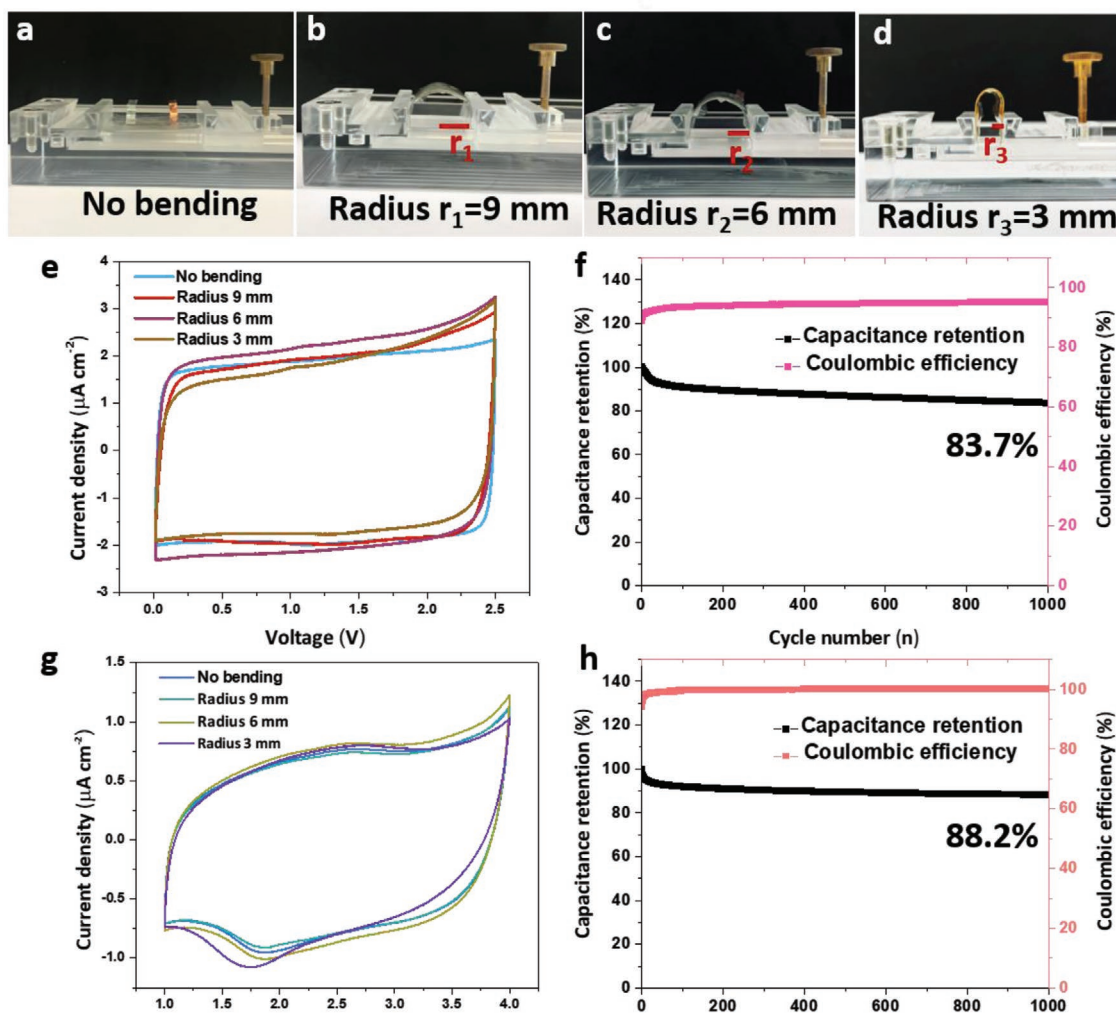


Figure 5. Photographs of a supercapacitor under a) no bending, b) bending radius of 9 mm, c) 6 mm, and d) 3 mm; CV curves of d) supercapacitor and f) hybrid supercapacitor under different bending radii and scan rates of 10 and 4 mV s^{-1} , respectively; Cycling performance of e) supercapacitor and g) hybrid supercapacitor under the bending radius of 6 mm.

in the literature on transparent supercapacitors based on carbonaceous materials with a variety of designs. Considering the combination of areal capacitance and transmittance, the performance metrics of the presented devices surpass several previous reports, as shown in Figure S14 and Table S2 (Supporting Information). For both the supercapacitor and hybrid supercapacitor, we found an acceptable balance between transmittance and areal capacitance. In addition, the hybrid supercapacitor outperforms the supercapacitor, because a high energy density can be achieved because of the faradaic process on the side of the anode (battery-type), whilst the high power density is a result of rapid non-Faradaic processes occurring in the cathode (capacitor type).

3. Conclusions

We have introduced micromolding as a powerful platform for the fabrication of transparent energy storage devices. Ag/porous

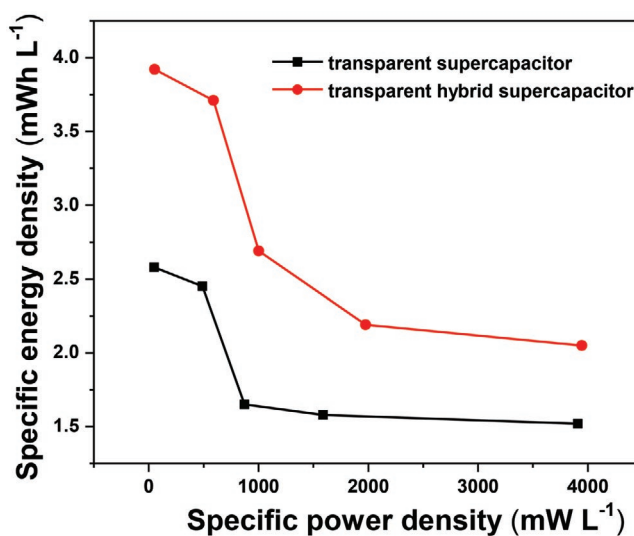


Figure 6. Ragone plot of the supercapacitor and hybrid supercapacitor.

carbon grids on PET substrates were successfully fabricated as transparent and flexible electrodes for supercapacitors. Porous carbon is positioned on top of a regular hexagonal Ag pattern, resulting in an electrode with a transmittance in excess of 80% at 550 nm. The unique regular architecture and aligned electrodes also guarantee high electrochemical stability of the supercapacitor over the typical potential window of 0–2.5 V. The symmetric Ag/porous carbon||Ag/porous carbon supercapacitor provides high areal capacitance, while maintaining a transmittance of 70.6% at 550 nm. The supercapacitor can be bent to a radius of 3 mm without losing the electrochemical stability over 1000 cycles. Significantly, the concept of micromolding has been extended to a second device, a Ag/Ni_xFe_yO_z@rGO electrode, which is highly promising as an anode for lithium-ion hybrid supercapacitors. By integrating two electrodes of Ag/porous carbon and Ag/Ni_xFe_yO_z@rGO, the hybrid supercapacitor offers high transparency, fast-charging capability and a long cycling life. These two examples represent proof-of-concept that micromolding has immense potential to be extended to other combinations of nano/micro-sized current collectors and active materials, with a view to developing highly transparent electrodes (based on regular grids) for use in transparent energy storage devices and next-generation electronics.

4. Experimental Section

Polydimethylsiloxane Stamp Fabrication: The fabrication process is shown in Figure S1 (Supporting Information). Briefly, the 2D grid was designed using AutoCAD 2014 (Autodesk, San Rafael, USA) and printed onto a film photomask (Micro Lithography Services Ltd, Chelmsford, United Kingdom). A 50 μm thick layer of negative photoresist SU-8 3050 (Microchem Corporation, Westborough, USA) was first spin-coated at 4000 rpm for 40 s on a 140 °C pre-heated silicon wafer (Siebert Wafer GmbH, Germany). The wafer was then soft-baked at 95 °C for 7 min. The photoresist layer was exposed for 38 s using a Karl Süss MA6 mask aligner (3.98 mJ cm⁻², 365 nm) and developed in 50 mL developer (Mr-Dev 600, Micro Resist Technology GmbH, Germany) for 5 min, generating a hexagonal photoresist mesh on the wafer. After rinsing in isopropanol, the wafer was baked at 95 °C for 6 min. Subsequently, this silicon wafer with the hexagonal photoresist mesh was glued to a Petri dish (diameter 100 mm) using an epoxy adhesive glue (Araldite Standard, Switzerland). A 10:1 mixture of PDMS elastomer and curing agent (Sylgard 184, Dow Corning, Midland, USA) was deposited on the patterned side of the silicon wafer, cured at 60 °C for 4 h and peeled off.

Synthesis of Ag Ink: Monodisperse silver nanoparticles were synthesized by reducing AgNO₃ with ethylene glycol according to a previous report.^[23] Specifically, 1.7 g polyvinylpyrrolidone (average M_w ≈ 55 000, Aldrich) was dissolved in 10 mL ethylene glycol (98% Technical, Pro Labo) and heated to 160 °C in an oil bath for 30 min. The color of the solution changed from colorless to light yellow over time. Then, 10 mL solution containing ethylene glycol and 0.17 g AgNO₃ (≥99.0%, Sigma-Aldrich) was added dropwise to the hot solution. The resulting mixture was kept at 160 °C for another 4 h until a brown dispersion was formed, indicating the formation of Ag nanoparticles. The dispersion was diluted to 50 mL with acetone and purified by eight cycles of centrifugation-redispersion (10 000 rpm, 20 min) using ethanol to remove the excess of PVP in the reaction mixture. To prepare the conductive nanoparticle ink, 500 mg of silver nanoparticles, obtained by drying the dispersion at 60 °C overnight, were re-dispersed into a mixture of 1 g ethylene glycol and 10 g ethanol by sonicating for 2 h.

Synthesis of Porous Carbon: Synthesis of porous carbon: Porous carbons were synthesized by a salt template method according to a

previous report.^[14] In a typical process, 30 mL aqueous solution of 5 g sucrose, 40 g ZnCl₂ and 0.55 g concentrated sulfuric acid was dried at 100 °C for 6 h and then kept at 160 °C for 6 h. The black mixture was then transferred to a tubular furnace for carbonization at 900 °C for 2 h, under a N₂ flow with a heating rate of 1 °C min⁻¹.

Synthesis of Ni_xFe_yO_z@rGO: Ni_xFe_yO_z nanoparticles were synthesized according to the published protocol.^[15] 2 mmol Fe (III) acetylacetonate (≥99.9%, Aldrich) and Ni (II) acetate tetrahydrate (99.998% trace metals basis, Aldrich) were added to 18.67 mL of benzyl alcohol (≥99.0%, Aldrich), sonicated then stirred until completely dissolved, and 1.33 mL of 1,3-propanediol (98%, Aldrich) were added into the solution. The obtained solution was then transferred into a 35 mL microwave glass tube. The reaction mixtures were heated to 160 °C for 30 min in a CEM Hybrid microwave reactor. The final product was centrifuged at 4000 rpm for 15 min. After collecting the supernatant and washing twice with diethyl ether, the obtained reddish-brown nanoparticles were dried at 60 °C, and finally redispersed in ethanol to achieve a concentration of 4 mg mL⁻¹. The reduced graphene oxide (rGO) was obtained by adjusting 70 mL of graphene oxide (GO) solution (5 mg mL⁻¹ in H₂O, Royal Elite, Shanghai, China) to a pH value of 10 using 30% ammonia, followed by adding 2 mL of hydrazine hydrate (50–60% N₂H₄, Aldrich) under magnetic stirring for 10 min. The solution was transferred to a 45 mL Teflon-lined stainless-steel autoclave (Parr Instrument Company, Moline, USA) and kept at 160 °C for 3 h. The rGO sheets were collected by centrifugation, rinsed with deionized water, and re-dispersed in ethanol to a concentration of 2 mg mL⁻¹. Finally, 20 mL of 4 mg mL⁻¹ Ni_xFe_yO_z and 20 mL of 2 mg mL⁻¹ rGO ethanol dispersions were mixed together and sonicated for 4 h in circulating water (Elmasonic P, frequency = 37 kHz, power = 100%).

Synthesis of Electrode Ink: Porous carbon and Ni_xFe_yO_z@rGO inks were prepared separately to ensure appropriate viscosity suitable for the micromolding method.^[24] Porous carbon and Ni_xFe_yO_z@rGO were dried at 80 °C overnight and mixed with polyacrylic acid (average M_w ≈ 1800, Aldrich) and water (mass ratio 14.55:0.45:100, total volume 10 mL). After ball milling at 30 Hz for 1 h, the electrode inks were kept at room temperature for the next steps.

Fabrication of Patterned Electrodes: Figure 1 graphically illustrates the fabrication process of the microstructured transparent porous carbon and Ni_xFe_yO_z@rGO grid electrodes. First, a 5 × 5 cm² polyethylene terephthalate film (0.05 mm thick, Toray) and a 3 × 3 cm² PDMS stamp (1 cm thick) were treated in O₂ plasma to obtain hydrophilic surfaces. The PDMS stamp was pressed against the PET film using a stainless-steel cylinder (780 g, diameter of 5 cm). 2 mL of Ag ink was then dropped by pipette around the edges of the PDMS stamp, followed by drying at room temperature for 30 min, baking at 60 °C for 1 h and sintering at 130 °C for 1 h to acquire good sheet resistance of the regularly patterned Ag films. Since the Ag and electrode inks consist of the low boiling point solvent (ethanol), at 60 °C the ethanol rapidly evaporates and forms a uniform film that efficiently prevents further spreading. In the following step, the electrode ink (both porous carbon and Ni_xFe_yO_z@rGO) was similarly applied on the edges of the PDMS stamp and then dried at 60 °C for about 30 min. After peeling off the PDMS stamp, the transparent micropatterned electrodes were obtained on the PET foils as a two layers architecture composed of Ag and porous carbon or Ni_xFe_yO_z@rGO.

Fabrication of Gel Electrolytes: The poly(vinylidene fluoride-hexafluoropropylene) (PVDF-HFP)/tetraethylammonium tetrafluoroborate (Et₄NBF₄) gel electrolyte was prepared according to a previous report.^[25] The electrolyte solution was prepared by dissolving 0.5 mol Et₄NBF₄ (99%, Aldrich) in 500 mL acetonitrile (99.9%, extra dry over a molecular sieve, Acros). 5 g of the host polymer (PVDF-HFP) (M_w ≈ 400 000, Aldrich) was separately dissolved in 30 g tetrahydrofuran by magnetic stirring at ≈ 60 °C. 15 wt% of liquid electrolyte was added to this solution. The resulting mixture was stirred at room temperature overnight to yield a homogenous solution. 2 mL of the solution was poured into a 3 cm diameter glass Petri dish. Tetrahydrofuran was allowed to evaporate at room temperature to form a self-standing and flexible gel electrolyte film with thickness ≈ 265 μm. A 1 M solution of

lithium bis(trifluoromethanesulfonyl)imide (LiTFSI, ≥99.0%, Aldrich) in a 1:1 mixture of ethylene carbonate (EC)/dimethyl carbonate (DMC) was made as the liquid electrolyte for hybrid-supercapacitors. The gel polymer electrolyte PVDF-HFP/LiTFSI was prepared by the above casting method similarly.

Battery Assembly: The two electrode films ($3 \times 3 \text{ cm}^2$) were fixed on opposite sides of a motorized x–y translation stage (Mad City Laboratories, Madison, USA) mounted on an inverted microscope (Nikon Ti-E Microscope, Zurich, Switzerland). The two films were mutually aligned in such a way that the pattern lay exactly on top of each other. After alignment, the two electrodes were separated by 5 cm, and then the gel electrolyte (diameter 3 cm) was placed in the middle. These three films were clipped tightly together and cut to a $2 \times 2 \text{ cm}^2$ footprint. Copper and aluminum strips were bonded to the anode and cathode films, respectively (Figure S9, Supporting Information). For packaging, a rectangular thermoplastic olefin bag ($3 \times 3 \text{ cm}^2$) with one side open and three sides sealed was fabricated by using a sealing machine (GN-HS200, Gelon, China) at $85 \text{ }^\circ\text{C}$ for 1 min. The electrolyte sandwiched by two electrodes was placed into the thermoplastic olefin bag. 30 μL of additional electrolyte was injected into the middle of the two electrodes to wet the gel electrolyte before sealing the fourth side of the thermoplastic olefin bag using a compact vacuum Sealer (GN-HS200V, Gelon, China) inside an argon-filled glovebox (H_2O , $\text{O}_2 < 0.1 \text{ ppm}$). The copper and aluminum strips protruded out of the bag to allow for further measurements. Before fabricating the hybrid supercapacitors, the as-prepared anode $\text{Ni}_x\text{Fe}_y\text{O}_z@\text{rGO}$ was prelithiated to reach the main insertion voltage of $\approx 0.7 \text{ V}$.

Characterization: X-ray diffraction measurements were performed on a PANalytical Empyrean equipped with a $\text{Cu K}\alpha$ X-ray tube (45 kV, 40 mA) and a monochromator. The morphology of the electrodes was studied by scanning electron microscopy on a LEO 1530 Gemini and by transmission electron microscopy on an X-FEG FEI Talos system. The 3D topography image and height profiles of electrode films were measured using an optical profilometer (Sensofar Plu Neox, Sensofar, Spain) in confocal mode. Topographical evaluation was carried out using the SensoMap software (v.6.0, Sensofar, Spain).

Electrochemical Measurements: To test the electrochemical performance of $\text{Ni}_x\text{Fe}_y\text{O}_z@\text{rGO}$ as an anode for lithium-ion batteries, $\text{Ni}_x\text{Fe}_y\text{O}_z@\text{rGO}$ electrodes were prepared by mixing 70 wt% of $\text{Ni}_x\text{Fe}_y\text{O}_z@\text{rGO}$ powders, 20 wt% carbon black and 10 wt% of polyvinylidene fluoride with *N*-methyl-2-pyrrolidinone under mechanical stirring. Electrochemical performances were evaluated in Swagelok-type cells, which were assembled in an argon-filled glovebox (H_2O , $\text{O}_2 < 0.1 \text{ ppm}$). For half-cell tests, Li metal was used as both counter and reference electrode together with a glass fiber as the separator and 1 M LiPF_6 in a 1:1 mixture of ethylene carbonate/dimethyl carbonate as the electrolyte. Cyclic voltammograms, galvanostatic charge-discharge curves, and electrochemical impedance spectroscopy data were recorded using an electrochemical workstation. All electrochemical measurements were performed using a Biologic instrument (BCS series) at room temperature. Electrochemical impedance spectroscopy measurements of the gel electrolytes PVDF-HFP/ Et_4NBF_4 and PVDF-HFP/LiTFSI were measured in a two-electrode system of the supercapacitor and hybrid-supercapacitor at an open circuit potential by applying alternating current potentials with a 5 mV amplitude in the frequency ranges from 10 mHz to 100 kHz, respectively. Ionic conductivity (σ) of the gel electrolytes was calculated from the bulk resistance according to Equation (1)

$$\sigma = \frac{L}{R_b A} \quad (1)$$

where L is the thickness of the electrolyte film (265 μm of PVDF-HFP/ Et_4NBF_4 and 257 μm of PVDF-HFP/LiTFSI) and A is the contact area of electrode–electrolyte interface ($2 \times 2 \text{ cm}^2$). The bulk resistance (R_b) of electrolytes can be estimated from the real part of impedance at high frequency of the semicircle. The areal capacitance, energy and power density are all based on the total area and volume of the supercapacitor and hybrid supercapacitor. GCD curves were applied at specific currents of 3, 60, and 120 $\mu\text{A cm}^{-2}$ in different cell voltage ranges (0–2.5 V for

the supercapacitor and 1–4 V for the hybrid supercapacitor). The areal gravimetric capacitance of the full-cell, C ($\mu\text{F cm}^{-2}$), was calculated according to Equation (2)

$$C = \frac{Q_{\text{dis}}}{(V - V_{\text{drop}})A} \quad (2)$$

where Q_{dis} (C) is the charge of the discharging cycle, V (V) is the discharging potential change, V_{drop} (V) is the voltage drop at the beginning of the discharge, and A ($2 \times 2 \text{ cm}^2$) is the electrode area in the full cell.

The energy density, E (Wh L^{-1}) and power density, P (W L^{-1}) of the full cells were estimated via Equations (3) and (4)

$$E = \frac{1}{2 \times 3.6 \times 5} C(V - V_{\text{drop}})^2 \quad (3)$$

$$P = \frac{E \times 3600}{\Delta t} \quad (4)$$

where V (V) is the discharging potential change, V_{drop} (V) is the voltage drop at the beginning of the discharge, S is the thickness of the full cell (765 μm for the supercapacitor, 910 μm for the hybrid supercapacitor) and Δt (s) is the discharging time.

Bending Tests: The mechanical properties of the Ag films as current collectors were evaluated using a specially designed tension/compression bending system. The tensile and compressive stress were carried out separately. Two copper tapes were bonded on two opposite sides of the Ag films, leaving a distance of 2 cm in between. The sheet resistance of the Ag films was measured during cyclic bending by a multimeter (Fluke Digital Multimeter 15B+). In addition, bending tests were performed to characterize the flexibility of the supercapacitors and hybrid supercapacitors. Figure 5a–d illustrates the bending setup and the different bending conditions (bending radii of 3, 6, and 9 mm). While being bent, the CV and GCD profiles of these devices were measured.

Supporting Information

Supporting Information is available from the Wiley Online Library or from the author.

Acknowledgements

The authors acknowledge ETH Zurich (ETH-50 19-2) and China Scholarship Council for financial support. The authors thank T. Kyburz for the help in producing the tool for the bending tests. The authors thank D. Han for helping with the photolithography process. The authors also thank the Scientific Center for Optical and Electron Microscopy (ScopeM) of ETH Zurich for providing the electron microscopy facilities.

Conflict of Interest

The authors declare no conflict of interest.

Keywords

flexible supercapacitors, micromolding, porous carbon, transparent hybrid supercapacitor, transparent supercapacitors

Received: May 22, 2020

Revised: July 6, 2020

Published online: September 9, 2020

- [1] a) X. Cai, M. Peng, X. Yu, Y. Fu, D. Zou, *J. Mater. Chem. C* **2014**, *2*, 1184; b) J. Gamby, P. L. Taberna, P. Simon, J. F. Fauvarque, M. Chesneau, *J. Power Sources* **2001**, *101*, 109; c) B. You, L. L. Wang, L. Yao, J. Yang, *Chem. Commun.* **2013**, 49, 5016.
- [2] a) K. Gao, Z. Shao, X. Wu, X. Wang, Y. Zhang, W. Wang, F. Wang, *Nanoscale* **2013**, *5*, 5307; b) X. Chen, X. Wu, S. Shao, J. Zhuang, L. Xie, S. Nie, W. Su, Z. Chen, Z. Cui, *Sci. Rep.* **2017**, *7*, 13239.
- [3] a) Y. Yang, S. Jeong, L. B. Hu, H. Wu, S. W. Lee, Y. Cui, *Proc. Natl. Acad. Sci. USA* **2011**, *108*, 13013; b) O. B. Wright, R. Li Voti, O. Matsuda, M. C. Larciprete, C. Sabilia, M. Bertolotti, *J. Appl. Phys.* **2002**, *91*, 5002; c) J. Y. Lee, S. T. Connor, Y. Cui, P. Peumans, *Nano Lett.* **2010**, *10*, 1276; d) J. Yoon, A. J. Baca, S. I. Park, P. Elvikis, J. B. Geddes, L. F. Li, R. H. Kim, J. L. Xiao, S. D. Wang, T. H. Kim, M. J. Motala, B. Y. Ahn, E. B. Duoss, J. A. Lewis, R. G. Nuzzo, P. M. Ferreira, Y. G. Huang, A. Rockett, J. A. Rogers, *Nat. Mater.* **2008**, *7*, 907.
- [4] a) A. P. Yu, I. Roes, A. Davies, Z. W. Chen, *Appl. Phys. Lett.* **2010**, *96*, 041109; b) T. Chen, Y. H. Xue, A. K. Roy, L. M. Dai, *ACS Nano* **2014**, *8*, 1039; c) P. Xu, J. Kang, J. B. Choi, J. Suhr, J. Y. Yu, F. X. Li, J. H. Byun, B. S. Kim, T. W. Chou, *ACS Nano* **2014**, *8*, 9437.
- [5] a) T. M. Higgins, J. N. Coleman, *ACS Appl. Mater. Interfaces* **2015**, *7*, 16495; b) T. Cheng, Y.-Z. Zhang, J.-D. Zhang, W.-Y. Lai, W. Huang, *J. Mater. Chem. A* **2016**, *4*, 10493; c) C. Zhang, T. M. Higgins, S.-H. Park, S. E. O'Brien, D. Long, J. N. Coleman, V. Nicolosi, *Nano Energy* **2016**, *28*, 495.
- [6] X. Y. Liu, Y. Q. Gao, G. W. Yang, *Nanoscale* **2016**, *8*, 4227.
- [7] a) M. A. Borysiewicz, M. Ekielski, Z. Ogorzalek, M. Wzorek, J. Kaczmarek, T. Wojciechowski, *Nanoscale* **2017**, *9*, 7577; b) I. Ryu, G. Kim, D. Park, S. Yim, *J. Power Sources* **2015**, *297*, 98; c) J. Rodriguez-Moreno, E. Navarrete-Astorga, E. A. Dalchiale, R. Schreiber, J. R. Ramos-Barrado, F. Martin, *Chem. Commun.* **2014**, 50, 5652.
- [8] a) J. Y. Lee, S. T. Connor, Y. Cui, P. Peumans, *Nano Lett.* **2008**, *8*, 689; b) H. Moon, H. Lee, J. Kwon, Y. D. Suh, D. K. Kim, I. Ha, J. Yeo, S. Hong, S. H. Ko, *Sci. Rep.* **2017**, *7*, 41981; c) H. Lee, S. Hong, J. Lee, Y. D. Suh, J. Kwon, H. Moon, H. Kim, J. Yeo, S. H. Ko, *ACS Appl. Mater. Interfaces* **2016**, *8*, 15449; d) S. Park, A. W. M. Tan, J. Wang, P. S. Lee, *Nanoscale Horiz.* **2017**, *2*, 199.
- [9] Y. Wang, S. Gong, D. S. Dong, Y. M. Zhao, L. W. Yap, Q. Q. Shi, T. An, Y. Z. Ling, G. P. Simon, W. L. Cheng, *Nanoscale* **2018**, *10*, 15948.
- [10] X. Huang, H. Zhang, N. Li, *Nanotechnology* **2017**, *28*, 075402.
- [11] J. L. Xu, Y. H. Liu, X. Gao, Y. Sun, S. Shen, X. Cai, L. Chen, S. D. Wang, *ACS Appl. Mater. Interfaces* **2017**, *9*, 27649.
- [12] T. Qiu, B. Luo, M. Giersig, E. M. Akinoglu, L. Hao, X. Wang, L. Shi, M. Jin, L. Zhi, *Small* **2014**, *10*, 4136.
- [13] J.-L. Xu, Y.-H. Liu, X. Gao, S. Shen, S.-D. Wang, *Energy Storage Mater.* **2019**, *22*, 402.
- [14] R. Y. Yan, M. Antonietti, M. Oschatz, *Adv. Energy Mater.* **2018**, *8*, 1800026.
- [15] H. J. Huang, X. Wang, E. Tervoort, G. B. Zeng, T. Liu, X. Chen, A. Sologubenko, M. Niederberger, *ACS Nano* **2018**, *12*, 2753.
- [16] H. J. Huang, M. Niederberger, *Nanoscale* **2019**, *11*, 19225.
- [17] L. Wei, Y. Fang, Y. F. Xu, X. Li, L. H. Li, *Sci. China: Technol. Sci.* **2014**, *57*, 2536.
- [18] T. C. Gao, Z. T. Li, P. S. Huang, G. J. Shenoy, D. Parobek, S. S. Tan, J. K. Lee, H. T. Liu, P. W. Lee, *ACS Nano* **2015**, *9*, 5440.
- [19] O. Zuas, N. Hamim, Y. Sampora, *Mater. Lett.* **2014**, *123*, 156.
- [20] P. Hao, Z. H. Zhao, J. Tian, H. D. Li, Y. H. Sang, G. W. Yu, H. Q. Cai, H. Liu, C. P. Wong, A. Umar, *Nanoscale* **2014**, *6*, 12120.
- [21] J. E. Lim, D. Y. Lee, H. K. Kim, *ECS J. Solid State Sci. Technol.* **2018**, *7*, P468.
- [22] T. F. Qiu, B. Luo, M. Giersig, E. M. Akinoglu, L. Hao, X. J. Wang, L. Shi, M. H. Jin, L. J. Zhi, *Small* **2014**, *10*, 4136.
- [23] T. Zhao, R. Sun, S. H. Yu, Z. J. Zhang, L. M. Zhou, H. T. Huang, R. X. Du, *Colloids Surf. A* **2010**, *366*, 197.
- [24] E. Kim, Y. N. Xia, G. M. Whitesides, *J. Am. Chem. Soc.* **1996**, *118*, 5722.
- [25] G. P. Pandey, S. A. Klankowski, Y. H. Li, X. S. Sun, J. Wu, R. A. Rojas, J. Li, *ACS Appl. Mater. Interfaces* **2015**, *7*, 20909.